Investigation of structural colors in *Morpho* butterflies using the nonstandard-finite-difference time-domain method: Effects of alternately stacked shelves and ridge density

Dong Zhu* and Shuichi Kinoshita
Graduate School of Frontier Biosciences, Osaka University, Suita 565-0871, Japan

Dongsheng Cai and James B. Cole
Graduate School of Systems and Information Engineering, University of Tsukuba, Tsukuba 305-8577, Japan
(Received 10 August 2009; published 30 November 2009)

We use the nonstandard-finite-difference time-domain (NS-FDTD) method to investigate the interaction of light with the complicated microstructures in the *Morpho* butterfly scales, which produce the well-known brilliant blue coloring. The NS-FDTD algorithm is particularly suitable to analyze such complex structures because the calculation can be performed in a short time with high accuracy on a relatively coarse numerical grid. We analyze (1) the microstructure obtained directly by binarizing an electron micrograph of the cross section of a scale, (2) the reflection and diffraction properties of three model structures—flat, alternating, and tree-shaped alternating multilayers, and (3) an array of alternating multilayers with random noise superposed on the height of the structures. We found that the actual microstructure well reproduced the reflection spectrum in a blue region by integrating the reflection intensities over all the reflection angles. Under normal incidence, the flat multilayer mainly stresses on multilayer interference except for shorter wavelengths, while alternating multilayer rather enhances the effect of diffraction grating due to longitudinally repeating structure by strongly suppressing the reflection toward the normal direction. In the array of alternating multilayers, the reflection into larger angles is considerably suppressed and the spectral shape becomes different from that expected for a single alternating multilayer. This suppression mainly comes from the scattering of reflected light by adjacent structures, which is particularly prominent for the TM mode. Thus a clear difference between the TE and TM modes is observed with respect to the origin of spectral shape, though the obtained spectra are similar to each other. Finally, the polarization dependence of the reflection and the importance of the alternating multilayer are discussed.

DOI: 10.1103/PhysRevE.80.051924 PACS number(s): 87.15.−v, 42.25.Fx, 78.40.−q

I. INTRODUCTION

Colors caused by the interaction of light with microstructures purely by physical means are collectively called structural colors; they are connected with various optical phenomena including scattering, diffraction, and interference [1–8]. In recent years, structural colors have aroused great attention for their applications in novel visual materials across varied industries such as fibers, paints, cosmetics, and jewels. In nature, structural colors are known to be commonly distributed in a wide variety of living beings with various sophisticated structural modifications.

One of the most well-known examples of structural colors is the famous *Morpho* butterfly [see Fig. 1(a)] found in Central and South America. The term "*Morpho* blue" originates from the color displayed by these butterflies, which belong to the genus *Morpho* and have attracted the attention of scientists for over a century [9–15].

The microstructures that contribute to the *Morpho* blue were elucidated after the invention of the transmission electron microscope (TEM). Anderson and Richards, Jr. [16] and Gentil [17] independently investigated the scales on *Morpho* butterfly and found the complex structures that contributed to the interference. Later, electron microscopic observations were reported by several authors [18–23]; they described clear multilayered structures, now called ridge-lamella or shelf structures [see Fig. 1(d)].

Subsequently, several detailed experiments on the reflectivity of the wing of *Morpho* butterfly were performed [24–37]. These experiments revealed not only the presence of a strong reflection band in the blue region but also an extraordinarily broad and anisotropic angular dependence; these properties were observed even at the single-scale level [24].

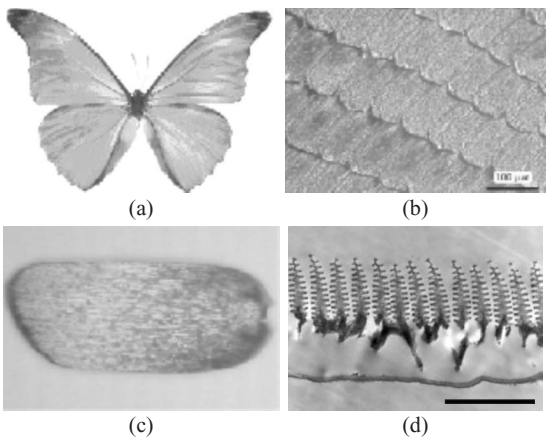

FIG. 1. (a) *Morpho rhetenor* and (b) an enlarged view of a wing covered with many scales. (c) An enlarged view and (d) a transverse cross section of a ground scale [24]. The scale bar in (d) is 3 μm.

*shu@fbs.osaka-u.ac.jp

 ©2009 The American Physical Society

However, the elucidation of the mechanism for *Morpho* blue has not progressed much since the beginning of the 20th century, and a simple model based on multilayer interference has long been utilized. Although this model is fairly good at predicting the wavelength that gives the maximum reflectivity, its major drawback lies in the angular dependence of the reflection: multilayer reflection only permits specular reflection. In principle, the reflectivity of a multilayer with an infinite width can be calculated analytically by several methods (e.g., Ref. [8]). However, treating a finite-width multilayer similarly is difficult because light is scattered and diffracted at each component of the multilayer; this results in the scattering of light over a wide angular range. Kinoshita *et al.* [26] derived an analytical model to calculate the angular dependence of the reflection from a finite-width multilayer under the assumption that each layer was infinitely thin, essentially neglecting the refraction and reflection of light at each layer. This model qualitatively explained the cooperative nature of interference and diffraction in the finite-width multilayer. However, the limitation in the applicability of this model was not fully discussed.

Various numerical calculation methods have been proposed to explain the peculiar optical properties of the *Morpho* butterfly wing; these methods include volume diffraction model [38], lamellar grating theory [39], and finite-difference time-domain (FDTD) method [29,40–42]. In particular, the FDTD method is quite powerful for deducing the interaction of light with the complex structures; it is able to calculate the electromagnetic fields both in the near- and far-field regions without the need for any particular assumption regarding the shape of the structure or the value of dielectric permittivity.

Using the FDTD method, Plattner [29] calculated the reflection properties for an array of various model structures—including flat multilayer, alternating multilayer, and tree-shaped structure—and reported the peculiar optical properties of the alternating multilayer structure. Banerjee *et al.* [40], on the other hand, utilized a high-accuracy version of the FDTD method called nonstandard-FDTD (NS-FDTD) [47] to calculate the reflection properties of the alternating multilayer. However, both Plattner and Banerjee *et al.* assumed that the model structures were arranged regularly, thus constituting a diffraction grating; this is far from the actual structure, which has a variety of irregularities. In order to truly understand the mechanism of *Morpho* blue coloration, a proper evaluation for irregularities is necessary because the irregularities are essential for evaluating the angular dependence of the reflection [26].

In this study, we employed the highly accurate NS-FDTD method to numerically calculate the reflectivity produced by the sophisticated microstructures in the *Morpho* butterfly wing and clarified the roles of these peculiar structures and irregularities. We focused on the following three points:

(1) Can microstructures obtained from a TEM image really reproduce the *Morpho* blue?

(2) What is the essential role of the alternating multilayer?

(3) How do the irregularities in an array of the structures affect its optical response?

In order to answer these questions, we investigated the optical responses for the following: (1) actual microstructure obtained directly by binarizing the TEM image of a *Morpho* butterfly scale, which naturally contains various irregularities; (2) three model structures—flat, alternating, and tree-shaped alternating multilayers; and (3) an array of alternating multilayers containing irregularities in the height of the model structure. Our result revealed that the alternating multilayer showed a strong reduction of reflection toward the normal direction under normal incidence, resulting in angular broadening particularly at shorter wavelengths. On the other hand, an array of alternating multilayers was found to have a special function depending on the polarization of incident light that reduced the reflection intensity at large reflection angles, particularly in the TM mode. In the following sections, we present the method and results of our calculations and compare the calculated results with those obtained by simple analytical models.

II. NS-FDTD METHOD

Since a general formalism of the FDTD method has been fully described in the literature [43,45,46], we only briefly review the essentials here. When an incident wave impinges on an object, the scattered electric field $\boldsymbol{E}_s$ and magnetic field $\boldsymbol{H}_s$ can be directly obtained by solving Maxwell's equations, which the FDTD method approximates using the following standard finite difference (SFD):

$$\partial_x f(x,y) \cong d_x f(x,y)/h, \tag{1}$$

where $d_x f(x,y)$ is the central finite difference defined by $d_x f(x,y)=f(x+h/2,y)-f(x-h/2,y)$. Hereafter, we limit our analysis to two-dimensional space because a major part of the reflection from the *Morpho* butterfly wing appears within a quasi-two-dimensional plane. Thus, in order to calculate the electromagnetic field in the two-dimensional space, we have to solve the equations at each grid point $\boldsymbol{x}=(x,y)$ on a domain using difference-approximated Maxwell's equations. The standard FDTD method is then given by

$$\boldsymbol{H}_s(\boldsymbol{x},t+\Delta t/2) = \boldsymbol{H}_s(\boldsymbol{x},t-\Delta t/2) - \frac{\Delta t}{\mu_0 h}\boldsymbol{d}\times\boldsymbol{E}_s(\boldsymbol{x},t), \tag{2}$$

$$\boldsymbol{E}_s(\boldsymbol{x},t+\Delta t) = \boldsymbol{E}_s(\boldsymbol{x},t) + \frac{\Delta t}{\epsilon(\boldsymbol{x})h}\boldsymbol{d}\times\boldsymbol{H}_s(\boldsymbol{x},t) - \frac{\epsilon(\boldsymbol{x})-\epsilon_0}{\epsilon(\boldsymbol{x})}\partial_t \boldsymbol{E}_0(\boldsymbol{x},t+\Delta t/2), \tag{3}$$

where Δt is the time step employed in this calculation and the replacement $\nabla\times\rightarrow\boldsymbol{d}/h\times$ is employed, where $\boldsymbol{d}$ is a vectorized differential operator corresponding to (d_x,d_y). μ_0 is the magnetic permeability of vacuum. The microstructure in the *Morpho* butterfly scale is believed to be of a nonmagnetic material, so the magnetic permeability of each grid point on the computational domain can safely be replaced by a constant μ_0. However, the permittivity $\epsilon(\boldsymbol{x})$ is a definite function of position $\boldsymbol{x}$. Thus, the refractive index $n(\boldsymbol{x})$ of the microstructure is related to only the permittivity as $\epsilon(\boldsymbol{x})=\epsilon_0 n^2(\boldsymbol{x})$, where ϵ_0 is the permittivity of vacuum. We used a plane wave as incident wave source to enable analytically compu-

tation for the third term on the right-hand side of Eq. (3).

The NS-FDTD method is derived by the replacement $\Delta t/h \rightarrow u(\boldsymbol{x})$ and $d \rightarrow d_0$ [45,47–49]; here, $u(\boldsymbol{x}) = \sin(\omega \Delta t/2)/v(\boldsymbol{x})\sin(kh/2)$, where ω is the angular frequency of the incident wave, k is the wave number, and $v(\boldsymbol{x})$ is the wave velocity that is a function of position $\boldsymbol{x}$. The velocity of the wave is expressed by the form of $v(\boldsymbol{x}) = c/n(\boldsymbol{x})$. d_0 is a new difference operator weighted by two independent difference operators.

In general, the refractive index of a scatterer has the complex form $n = n_r + in_i$, where n_r and n_i are the real and imaginary parts of the refractive index, respectively. In this case, the NS-FDTD method becomes

$$\boldsymbol{H}_s(\boldsymbol{x}, t + \Delta t/2) = \boldsymbol{H}_s(\boldsymbol{x}, t - \Delta t/2) - \frac{u_0(\boldsymbol{x})}{\mu_0} \boldsymbol{d}_0 \times \boldsymbol{E}_s(\boldsymbol{x}, t), \quad (4)$$

$$\boldsymbol{E}_s(\boldsymbol{x}, t + \Delta t) = \frac{1 - \tanh[\alpha(\boldsymbol{x})\Delta t]}{1 + \tanh[\alpha(\boldsymbol{x})\Delta t]} \boldsymbol{E}_s(\boldsymbol{x}, t) + \frac{u_0(\boldsymbol{x})}{\{1 + \tanh[\alpha(\boldsymbol{x})\Delta t]\}\epsilon(\mathbf{x})} \boldsymbol{d} \times \boldsymbol{H}_s(\boldsymbol{x}, t) - \frac{\epsilon(\boldsymbol{x}) - \epsilon_0}{\epsilon(\boldsymbol{x})} \partial_t \boldsymbol{E}_0(\boldsymbol{x}, t + \Delta t/2). \quad (5)$$

Here, the permittivity is given as $\epsilon(\boldsymbol{x}) = \epsilon_0[n_r^2(\boldsymbol{x}) - n_i^2(\boldsymbol{x})]$ and the absorption coefficient is given as $\alpha(\boldsymbol{x}) = n_r(\boldsymbol{x}) n_i(\boldsymbol{x}) \omega / \epsilon(\boldsymbol{x})$. $u_0(\boldsymbol{x})$ is derived as

$$u_0^2(\boldsymbol{x}) = \frac{\sin^2[\omega'(\boldsymbol{x})\Delta t/2] + \sinh^2[\alpha(\boldsymbol{x})\Delta t/2]}{v(\boldsymbol{x})\sin^2(kh/2)\cosh[\alpha(\boldsymbol{x})\Delta t]}, \quad (6)$$

where $\omega'^2(\boldsymbol{x}) = \omega^2 - \alpha^2(\boldsymbol{x})$.

In this calculation, the physical size of the computational domain is on the micron level. Thus, the electromagnetic field in the computational domain is that of a near field. To obtain the reflectivity in the far field, a near-to-far-field transformation [43,44] is naturally needed.

In general, the FDTD method derived by SFD has an error of $O[(h/\lambda)^2]$, where h is the grid size and λ is the incident wavelength. The error for the NS-FDTD method—where SFD is replaced by nonstandard-finite difference—can be considerably reduced to $O[(h/\lambda)^6]$ [47,49].

III. NS-FDTD METHOD APPLIED TO THE ACTUAL *MORPHO* BUTTERFLY SCALE

Morpho butterflies are well known for their brilliant blue wings. Of the various species, the male *Morpho rhetenor* (we abbreviate *M. rhetenor* hereafter) has the glossiest blue wings, which strongly stimulated our interest [Fig. 1(a)]. As shown in Figs. 1(b) and 1(c), the wing of *M. rhetenor* is covered with numerous flattened scales, which are 180–205 μm in length and 75–105 μm in width [50]. In general, *Morpho* butterfly wings are covered with two types of scales: cover and ground scales. However, in *M. rhetenor*, the cover scales are almost completely degenerated and only show their traces at the roots of the ground scales. Thus, the structural color in *M. rhetenor* is caused solely due to the ground scales.

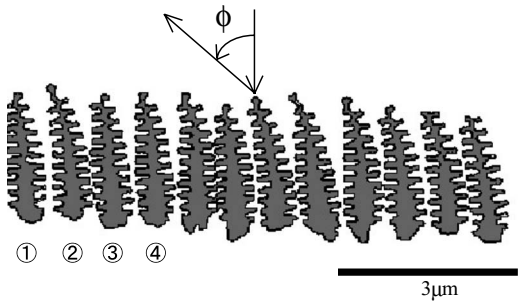

FIG. 2. Actual microstructure obtained by binarizing the TEM data for the transverse cross section of a *M. rhetenor* ground scale [24]. Scale bar is 3 μm. Numbers 1–4 are used in Fig. 3.

A ground scale of *M. rhetenor* is decorated by regularly lined ridges, which run in parallel with each other from root to tip of the scale with an interval of 600–670 nm [50]. These ridges are supported by many pillarlike structures, called trabecula, which are standing on a thin base plane. The ridges are further decorated by elaborate structures called lamellae or shelves [Fig. 1(d)]; usually 9–12 shelves are present in *M. rhetenor*. These shelves seem to be alternately stacked to the left and right sides of a central pillar. The strong blue coloring of this butterfly mostly originates from this elaborate shelf structure. Along the ridge, the shelves are obliquely attached with respect to a base plane, whose inclination angle is known as 7°–10° [27]. Thus, the upper ends of the inclined shelves can be easily seen from the top of the scale; they are rather randomly distributed, which implies irregularities for the height of the ridge [25,26]. The irregularity in the ridge height has been reported to cancel the interference among different ridges, resulting in the diffuse reflection within a plane normal to the ridge direction; in contrast, the angular range of the reflection along the ridge is rather strictly restricted [25–27]. This fact supports the extremely anisotropic reflection observed in this species of butterflies and thus confirms that such reflection takes place within a quasi-two-dimensional plane.

Here, we use two-dimensional NS-FDTD method to obtain the essential features of the reflection properties arising from such elaborate structures by comparing actual and model structures. Since the effectiveness of the NS-FDTD method has been fully demonstrated [45], including reports by our group [40,47–49], we first apply this method to an actual structure obtained directly from a TEM image of a *M. rhetenor* scale to confirm whether the TEM image can really reproduce the blue coloring. For this purpose, we scanned the TEM image reported by Vukusic *et al.* [24] and binarized it to obtain the computational model shown in Fig. 2. Since melanin pigments are known to be densely distributed at the lower part of each ridge, we removed them artificially and focused on the upper part, where only the shelf structures are clearly seen. In the NS-FDTD calculation, a plane wave is assumed to be normally incident on the structure from above the top of the ridge; we assumed a value of $1.56 + 0.06i$ as the refractive index of the ridges following the report by Vukusic *et al.* [24].

In Fig. 3, we first show the reflection properties in the TM mode from a single ridge using the NS-FDTD method. (We

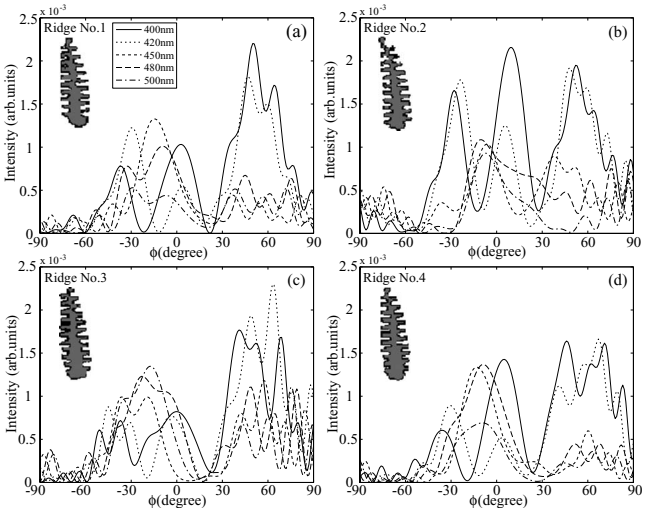

FIG. 3. Angular dependence of the reflection for various wavelengths from 400 to 500 nm in the TM mode. The ridge number shown in each figure corresponds to the ridge in Fig. 2. The calculations were performed with a mesh size of 10×10 nm^2.

denote the four ridges in Fig. 2 as Nos. 1–4, numbered from the left.) The angular dependence of the reflection from a single ridge is quite irregular owing to the structural irregularity. However, we can see from these figures that the angular range of the reflection is spread widely irrespectively of wavelength and that strong depressions of the reflection at around $\phi=20°$ can be observed for Nos. 1, 3, and 4. Considering that the ridges are slightly inclined to the left in the TEM image, we judged that the overall angular dependence is somewhat biased toward the positive angles. The results in the TE mode were similar to those in the TM mode, but the angular range was slightly restricted. At a glance, it is rather difficult to directly derive any important features from these complex patterns. We overcame this difficulty by integrating the reflection intensity over a wide angular range from −90° to +90°. Figure 4 shows the angle-integrated spectra thus obtained for a total of 12 ridges. In spite of the randomness

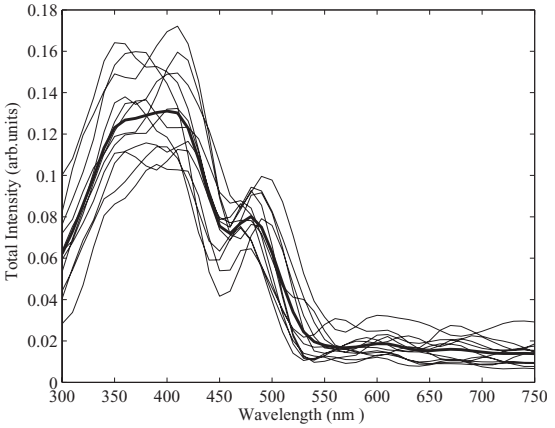

FIG. 4. Angle-integrated reflection spectra for 12 individual ridges in Fig. 2 in the TM mode. A thick solid line shows an average of 12 spectra. The calculations were performed with a mesh size of 10×10 nm^2.

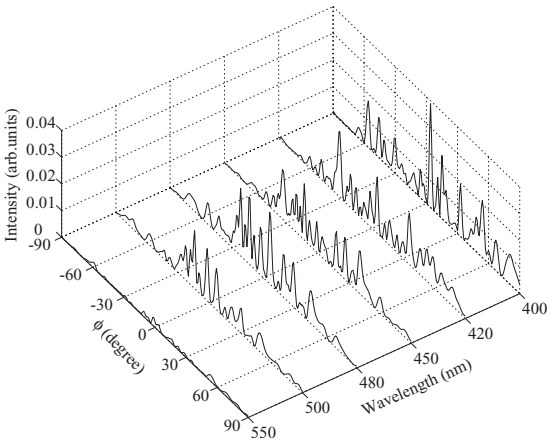

FIG. 5. Angular dependence of the reflection intensities at wavelengths of 400, 420, 450, 480, 500, and 550 nm calculated for the structure shown in Fig. 2 under normal incidence. The calculations were performed with a mesh size of 10×10 nm^2.

found in the angular dependence, the integrated spectra for individual ridges were rather similar to each other, showing a peak around 350–410 nm with a small shoulder around 480 nm.

Next, we applied the NS-FDTD method to the array of ridges shown in Fig. 2. In Fig. 5, we show the angular dependence of the reflection at various wavelengths from 400 to 550 nm for the TM mode under normal incidence condition. It is clear that strong reflection was observed for the wavelength range of 400–500 nm, with severe irregularity in the angular distribution. This type of irregularity is often observed when a natural product or an object with artificially introduced irregularity is employed as a sample for light scattering; it is considered to arise from the interference effect among ridges having considerable irregularities, which is similar to the well-known laser speckle pattern. This is partly because only a small number of ridges are taken into account in the calculation. This type of complex reflection pattern has actually been reported for single-scale experiments, where only several tens of ridges were sampled [24].

To overcome this, we calculated the angle-integrated reflection spectrum again. Figure 6 shows the spectrum thus obtained, which we compared with the experimentally obtained spectrum using an integrating sphere [26]. Since the experiment referred to here was performed under unpolarized conditions, we averaged the reflection spectra for the TM and TE modes equally to enable a direct comparison with the experimental results. Although the spectral shape for the TM mode was slightly broader than that for the TE mode, their sum reproduced the experimental observation fairly well, including the spectral width, although a slight peak shift and a large distortion can be seen in the calculated spectrum. The distortion may possibly be attributed to the inhomogeneity in ridge shapes; furthermore, the number of ridges employed is considerably smaller so that the statistical fluctuation is not canceled. Thus, we confirmed that the NS-FDTD method is effective for analyzing systems containing considerable irregularities, such as the butterfly scales in nature.

Comparing the results for an array of ridges with that for a single ridge, we noticed a considerable peak shift. Namely,

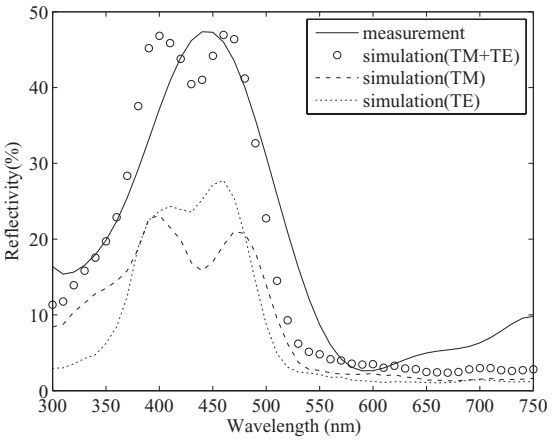

FIG. 6. Angle-integrated reflection spectrum calculated for the structure shown in Fig. 2 under normal incidence (open circles). The solid line is the angle-integrated reflection spectrum measured using an integrating sphere for *M. rhetenor* [26]. In order to compare the simulation with the experiment, the calculated results for the TM (dashed line) and TE modes (dotted line) were added equally. The calculations were performed with a mesh size of 10 $\times 10$ nm^2.

the peak calculated for the array lies at around 430 nm, while that for the single ridge is at around 380 nm. This is quite interesting because if we consider a simple diffraction grating theory—where an array of ridges and the ridge heights are considered to be sufficiently random to cancel the interference among ridges—the angular dependence of the diffraction intensity becomes a simple sum of that for single ridge diffraction. Thus, a peak shift or a considerable suppression at a shorter wavelength range implies that complex interactions are present within the array of ridges. In later sections, we discuss this point using the model system shown below.

IV. MODEL CALCULATIONS AND ANALYSES

A. Analyses of model structures

Using various model structures, we derived the essential features of the ridge structures that cause the characteristic blue reflection. First, we investigated the three model structures shown in Fig. 7: (a) flat multilayer, (b) alternating multilayer, and (c) tree-shaped alternating multilayer. The layers employed here were assumed to consist of cuticles with a refractive index of $1.56+0.06i$, while the remaining regions were filled with air, which has a refractive index of 1.0. We specified the following fundamental parameters for the calculations according to the previous work [26]: the total width and thickness of the cuticle layer are 300 and 55 nm, respectively, with a layer spacing of 150 nm and 9 cuticle layers. For the alternating multilayer, one of the two half-layers was shifted vertically by 118 nm, corresponding to half of the optical path length between the two adjacent cuticle layers. A tree-shaped alternating multilayer was constructed by assuming an equilateral triangle with a base length of 300 nm and height of $(55+150)\times 9=1845$ nm. This triangle was laid on an alternating multilayer model,

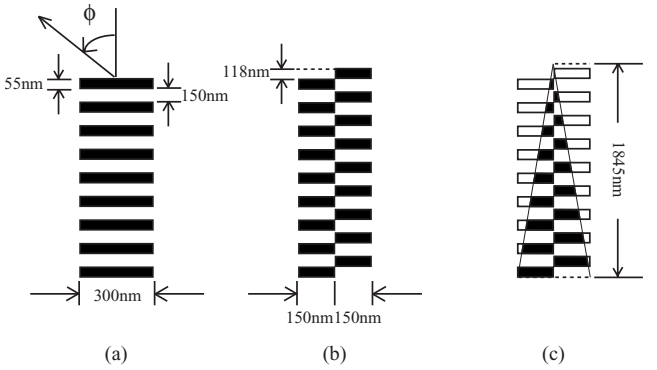

FIG. 7. (a) Flat, (b) alternating, and (c) tree-shaped alternating multilayers.

and the overlapped region was then clipped. A plane wave was then assumed to be normally incident on the structures, and the grid size was determined as 10 nm, so that the simulated results would not change further with a decrease in grid size.

The left column of Fig. 8 shows the angular dependence of the reflection intensities corresponding to the above three models. In Fig. 8(a), we noticed that the flat multilayer shows a strong reflection toward the normal direction over a wide wavelength range from 420 to 480 nm, for which the

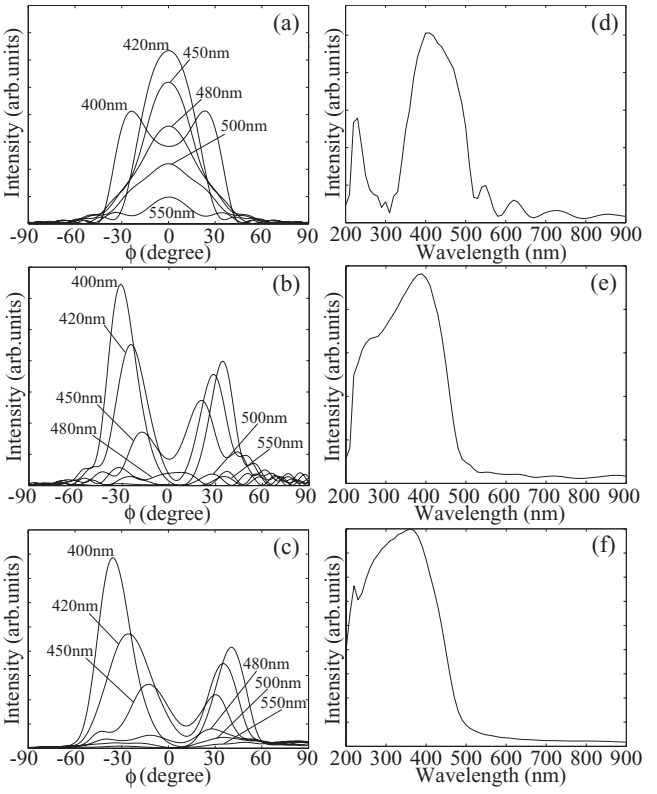

FIG. 8. Angular dependence of the reflection intensities from the following three model structures under normal incidence at various incident wavelengths: (a) flat multilayer, (b) alternating multilayer, and (c) tree-shaped alternating multilayer. (d)–(f) Angle-integrated reflection spectra for the three model structures. The calculations were performed with a mesh size of 10×10 nm^2.

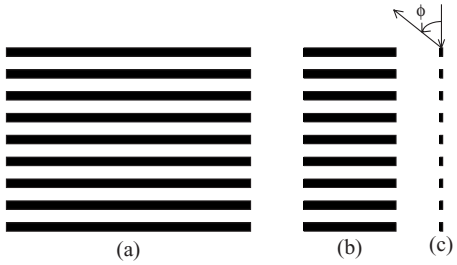

FIG. 9. (a) Multilayer with an infinite width, (b) flat multilayer model, and (c) diffraction grating.

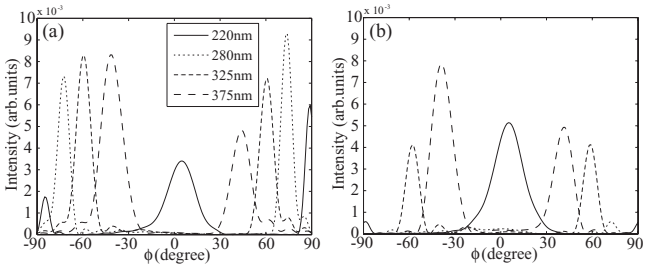

FIG. 10. Angular dependence of the reflection intensities of an alternating multilayer at shorter wavelengths under normal incidence in the (a) TM and (b) TE modes. The calculations were performed with a mesh size of 10×10 nm^2.

angular range was extended to over $\pm20°$. These spectral and angular distributions indicate that multilayer interference and diffraction due to the finite width of the layer take place simultaneously. In Fig. 8(d), we show the angle-integrated reflection spectrum for the flat multilayer. The two peaks observed at around 400 and 220 nm correspond to the first- and second-order reflection bands, respectively, if multilayer interference is assumed.

For the first-order peak, the wavelength giving the maximum reflection intensity was located at about 400 nm, which differs considerably from the estimated value of $\lambda_m=471.6$ nm from the optical path length between two adjacent layers through the ordinary relation of multilayer interference $2(n_1d_1+n_2d_2)=\lambda_m$. Here, λ_m is the wavelength giving the peak of the first-order reflection band, $n_1=1.56$ and $n_2=1.0$ are real parts of the refractive indices for the cuticle and air layers, respectively, and $d_1=55$ nm and $d_2=150$ nm are their thicknesses. This is partly because the diffraction effect that causes the emission of light toward oblique directions contributes to the enhancement of shorter wavelength components and also because the refractive index of the cuticle layer has an imaginary part. For the former, our calculations show that the reflection band center actually shifts from ~480 to ~425 nm when we compare the reflection peak for a multilayer with an infinite width with that for the present flat multilayer model without considering the imaginary part. On the other hand, in the latter, a similar spectral shift is observed for the reflection spectrum from multilayer interference with an infinite width. A simple calculation for an infinite multilayer shows that a shift in the reflection peak occurs from ~480 to ~430 nm when the refractive index is changed from 1.56 to $1.56+0.06i$.

At a wavelength of 400 nm, the angular dependence of the reflection intensity shows peaks at around $\pm24°$. A qualitative explanation of this effect is possible if we consider that the flat multilayer model employed here takes an intermediate form between the following two extrema: a multilayer with an infinite width and an extremely thin diffraction grating, as shown in Figs. 9(a) and 9(c), respectively. Since the reflectivity from multilayer interference with an infinite width falls to a minimum at around 400 nm, the effect of diffraction grating may play a central role in the angular distribution. This effect was roughly estimated using the relation $n_2(d_1+d_2)(1+\cos\phi)=\lambda_d$, where ϕ is the reflection angle and λ_d is the wavelength that gives the first-order diffraction peak. The calculation of this relation gives the first-order diffraction peak as located at $\phi=18.0°$ for $\lambda_d=400$ nm, which is somewhat smaller but comparable with the exact result based on the NS-FDTD calculation of 24°.

Figure 8(b) shows the angular dependence of the reflection intensity for the alternating multilayer. A remarkable difference was found as compared with that for the flat multilayer. To be specific, the reflection toward the normal direction was strongly suppressed, while that to the oblique direction of around 20°–40° was largely enhanced. We also noticed that the angle giving the maximum reflection gradually increased when the wavelength was decreased; this was more prominent at shorter wavelengths, as shown in Fig. 10.

The peculiar suppression of the reflection intensity toward the normal direction is easily explained in terms of the destructive interference of the reflected light from the left and right half-layers. The light reflected from these layers has a phase difference of 180° when the wavelength satisfies the relation $\lambda=4d_{\text{diff}}$ (d_{diff} is the optical path length difference between the two layers), which is then related to the height difference. Since we set $d_{\text{diff}}=118$ nm, the reflection toward the normal direction is strongly suppressed at around 470 nm. A similar phenomenon was actually observed in the reflection measurements for a single scale of *M. rhetenor* [24].

The shift of the peak position in the angular dependence can be roughly estimated using the diffraction grating theory, as described above, in which Kirchhoff's inclination factor ($\sin^2\phi$ in this case) is further included. In this theory, the first-order diffraction peak is only observable below ~410 nm and appears at the reflection angles of 20° and 27° for 420 and 400 nm, respectively; these values are comparable with 25° and 30° observed in the FDTD calculation. The diffraction effect is stronger when the wavelength becomes shorter because Kirchhoff's inclination factor becomes larger when the reflection angle is increased. This effect is particularly prominent for the TM mode, as shown on the left-hand side of Fig. 10; in the TE mode, the reflection at larger angles is strongly suppressed. We later discuss the positions of these peaks in conjunction with another diffraction grating formed by an array of ridges. At the wavelength of 220 nm, a peak was found to appear near the normal direction. This is because an alternating multilayer actually provides destructive interference at around 470 nm but constructive interference at around 235 nm.

The angle-integrated reflection spectrum in Fig. 8(e) shows a maximum at a shorter wavelength of around 390 nm. In addition, a considerable increase in the reflection in-

tensity was observed at around 300 nm, where there is a broad dip for the flat multilayer. This mainly arises from the diffraction grating effect mentioned above; the effect of multilayer interference is strongly suppressed, owing to the destructive interference of the multilayer in this wavelength range, which is consistent with the strong peak found in the angular dependence of the reflection intensity. In summary, the alternating multilayer highlights shorter wavelengths and broadens the angular range of reflection by sacrificing the reflection toward the normal direction.

Figures 8(c) and 8(f) show the angular dependence of the reflection intensity and angle-integrated reflection spectrum for the tree-shaped alternating multilayer. The overall profile is very similar to the normal alternating multilayer except that the angular distribution is somewhat broader and the angle-integrated reflection spectrum becomes less pronounced. Thus, we focused mainly on the peculiar features observed in the alternating multilayer [Fig. 7(b)].

B. Comparison with analytical model

Before continuing with the analyses, we briefly comment here on the analytical model proposed for the flat multilayer by one of the present authors [25,26]. Kinoshita *et al.* proposed a simple analytical model to express the cooperative effect of multilayer interference and diffraction under the assumption that the thickness of the cuticle layer is extremely small; therefore, the incident and reflected lights do not suffer from any reflection nor refraction by the other layers. They calculated the angular dependence using the following parameters: a layer width of 300 nm, thickness of 55 nm, layer interval of 205 nm, and number of layers equal to 6 with the refractive index of 1.55. They adjusted the layer interval to be consistent with the optical path length between two adjacent layers. Employing the same parameters, we performed the NS-FDTD calculations and compared our results with those obtained by the analytical model. The result is shown in Fig. 11. The NS-FDTD method clearly gives a much stronger reflection toward the normal direction than the analytical model, as shown in Figs. 11(a) and 11(c). This is because the analytical model assumes an ensemble of infinitely thin layers, so it eventually ignores the multiple reflections among the layers. If we change the refractive index of the layer from 1.55 to 1.01 to reduce the surface reflection while keeping the optical path length constant, the NS-FDTD method actually reproduces the angular dependence obtained by the analytical model, as shown in Fig. 11(b). This comparison clearly shows the limitation of the analytical model and the usefulness of the NS-FDTD method when applied to such complex structures. However, it should be noted that the measured result for the *M. didius* wing after removing the cover scales was somewhat close to the analytical result [Fig. 11(d)] [26].

V. ANALYSES OF AN ARRAY OF ALTERNATING MULTILAYERS

Next, we considered an array of alternating multilayers, as shown in Fig. 12. We arranged a total of ten alternating multilayers equidistantly and took into account the irregularity in the height of the structure, which is denoted as Δy.

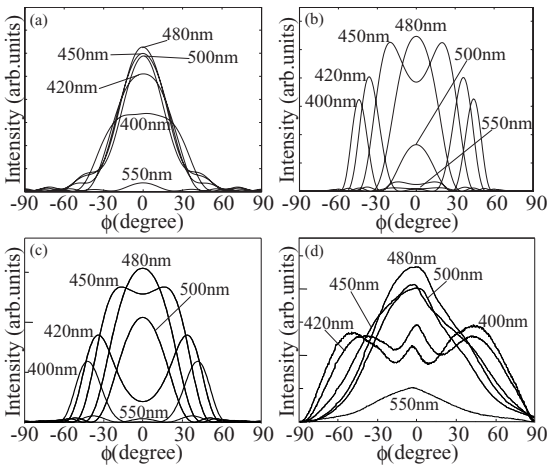

FIG. 11. (a) Angular dependence of the reflection intensities of a flat multilayer calculated by the NS-FDTD method with a layer width of 300 nm, thickness of 55 nm, spacing between two adjacent layers of 150 nm, number of layers equal to 6, and refractive index of 1.55 from Ref. [26]. (b) Calculated result for a refractive index of 1.01 while the optical path length between adjacent layers is kept constant. (c) Calculated result by using the analytical model and (d) measured result for a *M. didius* wing after removing the cover scales [26]. The calculations for (a) and (b) were performed with a mesh size of 10×10 nm^2.

A. Regular array of alternating multilayers

First, we show in the left-hand side of Fig. 13(a) the angular dependence of the reflection intensities in the TM mode from regularly arranged structures at several wavelengths under normal incidence. This calculation is essentially equivalent to the FDTD calculation performed by Plattner [29] and the NS-FDTD calculation carried out by Banerjee *et al.* [40]. When the alternating multilayers are regularly arranged, a diffraction grating is formed, in which each alternating multilayer works as a unit scatterer. Thus, under normal incidence, diffraction spots appear at the angles that satisfy the relation $d \sin \phi = m\lambda$, where d is the distance between two adjacent alternating multilayers. For instance, when a wavelength of 400 nm is employed, the first-order diffracted light should appear at $\phi = 36.9°$, which agrees quite well with the computational result. We also noticed that the zeroth-order diffracted light is remarkably sup-

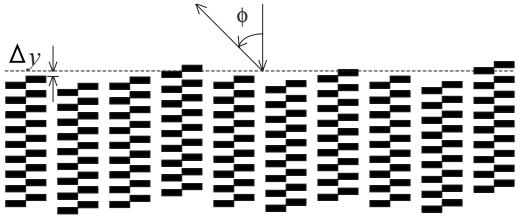

FIG. 12. Model for an array of alternating multilayers with random heights. The deviation from a mean value of the ridge height is denoted as Δy.

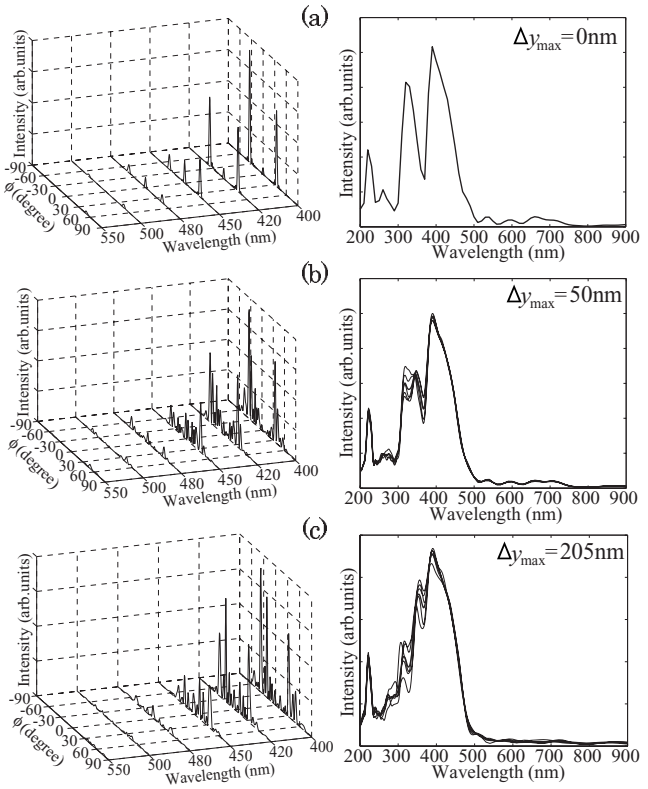

FIG. 13. Angular dependence of the reflection intensities (left) and angle-integrated reflection spectra (right) of an array of alternating multilayers with irregularity in the ridge height. The irregularity was introduced by giving a uniform random number within a maximum range of $\pm\Delta y_{max}$, where $\pm\Delta y_{max}$=(a) 0, (b) 50, and (c) 205 nm. In (b) and (c), the angle-integrated spectra were calculated for five series. The five curves and their average are plotted as thin and thick curves, respectively. The calculations were performed with a mesh size of 10×10 nm^2.

pressed near 400 nm. This is because a single alternating multilayer largely suppresses the reflection toward the normal direction in that wavelength. We also found that the reflection at shorter wavelengths seems to be rather enhanced.

On the right-hand side of Fig. 13, we show the angle-integrated reflection spectrum for a regular array of alternating multilayer, which shows three prominent peaks at 220, 325, and 400 nm. The origin of these peaks can be easily understood if we consider the angular dependence of the reflection intensity for a single structure and the effect of diffraction grating; this is because the diffraction properties of a simple diffraction grating are generally expressed as a product of the properties of a single structure that constitutes the grating and a diffraction grating composed of an array of scattering points. In Fig. 14, the angular dependence of the reflection intensities for a single ridge and an array of regularly arranged ridges are compared at the above three wavelengths. We confirmed that at 400 nm, the first-order diffraction spots overlap only with the reflection pattern of a single structure, and thus the first-order diffraction is mainly responsible for the peak. On the other hand, at 325 nm, the second-order diffraction spots overlap with that of a single

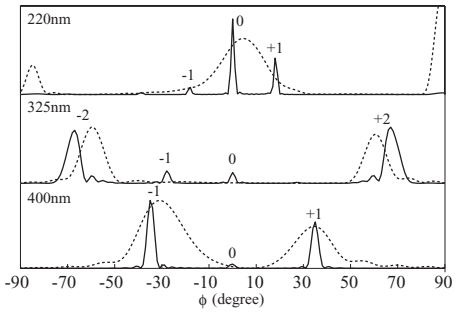

FIG. 14. Angular dependence of the reflection intensities of a single ridge (dashed line) and an array of regularly arranged ridges (solid line) with a spacing of 700 nm at the wavelengths of 220, 325, and 400 nm, where the angle-integrated reflection spectrum shows peaks. The diffraction orders corresponding to the peaks of the reflection intensities are indicated as positive or negative numbers.

structure, while at 220 nm, both the zeroth- and first-order peaks are responsible for the spectrum.

These overall properties can be understood more intuitively if we plot the relation between the wavelength and the reflection angle. In Fig. 15, the zeroth-, first-, second-, and third-order diffraction spots are expressed as solid lines, while the reflection peak due to a single alternating multilayer is illustrated as a shaded area, where the central thick line indicates the peak of the reflection intensity, which is obtained by interpolating the data at several wavelengths using a polynomial function, while two thin lines indicate the range of reflection band expressed as the positions at half of the peak intensity. The density of colors roughly expresses the reflection intensity. Note that the small area at around 225 nm originates from the second-order multilayer interfer-

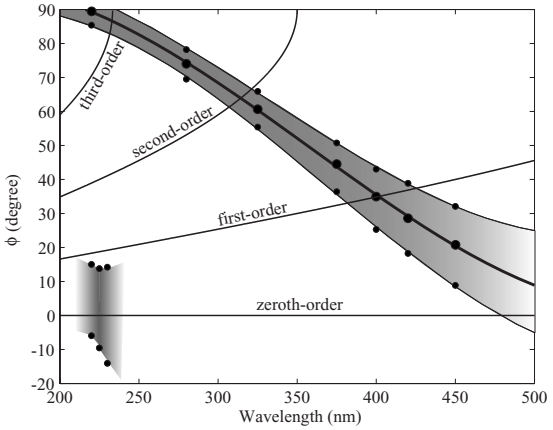

FIG. 15. Angular dependence of the diffraction spots of various orders for a spacing of 700 nm (thin solid lines) and of the reflection peaks for a single alternating multilayer (shaded area). The thick solid line indicates the peak position of the reflection intensity obtained by interpolating the data shown in closed circles, while the thin solid lines indicate the bandwidths evaluated at half of the height of the reflection bands. The density of the shade roughly expresses the reflection intensity. Note that the overlapping regions of these curves give peaks in the angle-integrated reflection spectrum shown in Fig. 13(a).

ence, which appears as the reflection toward the nearly normal direction. The overlap of these diffraction spots and reflection bands due to a single structure produces a peak in the angle-integrated reflection spectrum. This figure indicates that the first-order diffraction occurs at around 380–430 nm and a reflection angle of ~35°, while the second-order diffraction occurs at around 310–325 nm and an angle of ~64°. On the other hand, at around 220 nm, the zeroth- and third-order diffraction spots overlap with each other. This expectation agrees well with the angle-integrated reflection spectrum calculated for an array of alternating multilayers.

B. Array of alternating multilayers with irregularity

Next, we introduced irregularity into the heights of an array of regularly arranged alternating multilayers. The irregularity in the ridge heights for actual *Morpho* butterflies is believed to diffuse the reflected light by disturbing the interference of the reflected light by various ridges; thus the reflection properties for a single ridge can be directly attributed to the reflection from a *Morpho* scale [25]. In order to introduce the irregularity in the model calculation, we first define the height of the jth ridge as Δy_j, which was measured from the average height of the ridges. Then, the height values were produced by generating uniform random numbers within a maximum range of $\pm\Delta y_{\max}$. Figures 13(b) and 13(c) show the angular dependence and angle-integrated spectra for an array of alternating multilayers with maximum irregularities, $\Delta y_{\max}$, of 50 and 205 nm, respectively. With increasing irregularity in the ridge height, the diffraction spots that clearly appear in Fig. 13(a) fade out quickly; the angular dependence is finally expressed as an ensemble of random peaks, which resembles the result calculated for actual ridge structures (see Fig. 5). The envelope of the random peaks reminds us of the angular dependence of a single alternating multilayer for which the reflection toward the normal direction is strongly suppressed. As described above, these disordered reflection patterns are characteristic of light scattering due to randomly distributed structures.

The right-hand side of Fig. 13 shows the angle-integrated reflection spectra, where the results for five series of calculations and their average are plotted. In spite of the disordered peaks for the angular dependence, relatively smooth curves are always obtained by integrating over all the reflection angles from −90° to 90°. It is remarkable that the peak appearing at 320 nm for the regular array is largely suppressed as the magnitude of the irregularity is increased; it is finally buried within a smooth slope on the short-wavelength side of the reflection spectrum. On the other hand, the peaks at around 400 and 220 nm remain rather constant. We also noticed that the spectral shape within the range of 220–400 nm is considerably influenced by the random numbers employed but does not depend on the choice of the random numbers outside this range.

Within the framework of a simple grating theory, the diffracted light field from N regularly arranged structures with a height difference of Δy_j for the jth structure, which is measured from the average height, is expressed as

$$E = f(\theta,\phi)\sum_{j=0}^{N-1} e^{ikjdu}e^{ik\Delta y_j v}, \tag{7}$$

where $f(\theta,\phi)$ is the angle-dependent diffraction efficiency and includes Kirchhoff's inclination factor with $u=\sin\theta+\sin\phi$ and $v=\cos\theta+\cos\phi$. k and d are the wave numbers of the light and the spacing of the structures, respectively. If the irregularity is introduced in the height of the structure and the diffracted light is assumed to be statistically averaged, the following relation is easily derived:

$$\begin{aligned}\langle|E|^2\rangle &= |f(\theta,\phi)|^2\left\langle\sum_{j,l=0}^{N-1} e^{ik(j-l)du}e^{ik(\Delta y_j-\Delta y_l)v}\right\rangle \\ &= |f(\theta,\phi)|^2\left\{N+\sum_{j,l(j\neq l)}^{N-1} e^{ik(j-l)du}\langle e^{ik(\Delta y_j-\Delta y_l)v}\rangle\right\} \\ &= |f(\theta,\phi)|^2\left\{N+\alpha\left(\sum_{j,l}^{N-1} e^{ik(j-l)du}-N\right)\right\} \\ &= |f(\theta,\phi)|^2\left\{N(1-\alpha)+\alpha\left(\frac{\sin kNdu}{\sin kdu}\right)^2\right\},\end{aligned} \tag{8}$$

where $\alpha\equiv|\langle e^{ik\Delta yv}\rangle|^2$ expresses the degree of the irregularity, which is dependent both on the magnitude of the irregularity introduced and on the incident and reflection angles. This formula indicates that the complete irregularity of $\alpha=0$ corresponds to when the diffraction properties are completely expressed as a simple sum of the single-structure diffraction. On the other hand, the other extreme of $\alpha=1$ is for when diffraction spots are clearly seen; the spots are then modified by the diffraction properties for a single structure. In the intermediate case, the diffraction properties are expressed as a sum of these two.

The parameter α is easily evaluated if we consider that Δy_j is given by uniform random numbers within a range of $\pm\Delta y_{\max}$,

$$\begin{aligned}\alpha &\equiv |\langle e^{ik\Delta yv}\rangle|^2 \\ &= \left|\int_{-\Delta y_{\max}}^{\Delta y_{\max}} e^{ik\Delta yv}d\Delta y \Big/ \int_{-\Delta y_{\max}}^{\Delta y_{\max}} d\Delta y\right|^2 \\ &= \left(\frac{\sin(k\Delta y_{\max}v)}{k\Delta y_{\max}v}\right)^2.\end{aligned} \tag{9}$$

In Fig. 16, we plot α against the reflection angle for various values of $\Delta y_{\max}$ under normal incidence. α is definitely dependent on the reflection angle and generally increases as the absolute value of the angle is increased. The irregularity of $\Delta y_{\max}=50$ nm employed in Fig. 13(b) gives only a small effect on reducing the interference between ridges, particularly at large reflection angles. On the other hand, the irregularity of $\Delta y_{\max}=205$ nm, which corresponds to the layer interval of our model, removes the interference effect almost completely so that α lies within 0.03 for all the reflection angles. We can safely conclude that the angle-integrated spectrum, obtained when irregularity $\Delta y_{\max}=205$ nm, is almost completely free from the interference due to the reflection from adjacent ridges.

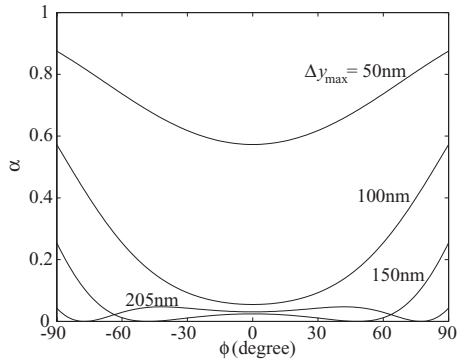

FIG. 16. Angular dependence of α for various values of $\Delta y_{\max}$.

C. Effect of polarizations

We then compared the angle-integrated spectrum obtained for ten ridges with that for a single ridge. We show the results in Fig. 17, where we normalize both spectra at their peaks. The left-hand side of the figure shows the result for the TM mode. We found that these two spectra differ considerably, particularly in a range of 220–400 nm, while above and below this range the spectra agree considerably well with each other. On the other hand, in the TE mode, the difference is quite small and their overall shapes somewhat resemble that of the TM mode for ten ridges, although the reflection intensity at 220 nm is relatively large in the former.

Considering that the reflection within the wavelength range of 220–400 nm occurs at large reflection angles above 30° (see Fig. 15) and further that the TE mode under normal incidence basically provides a small contribution to the reflection at large angles, we speculated that the reflected light at large reflection angles is considerably disturbed by adjacent ridges owing to scattering or absorption; the contribution of the adjacent ridges is so large that even the overall spectral shape is changed.

To confirm this, we performed the NS-FDTD calculations on the ridge-interval dependence of angle-integrated reflection spectra for ten alternating multilayers with a height irregularity of $\Delta y_{\max}=205$ nm for the TM mode. We evaluated the change in the reflection spectrum by comparing the reflection intensities for an incident wavelength of 320 nm

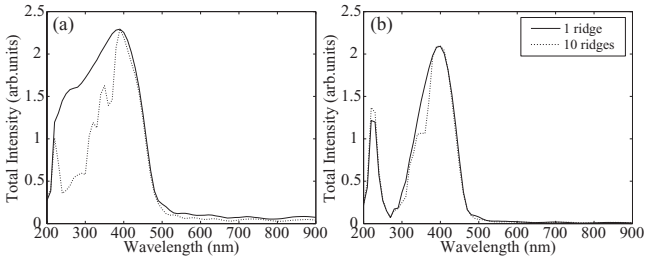

FIG. 17. Angle-integrated reflection spectra in the (a) TM and (b) TE modes for a single alternating multilayer (solid line) and an array of ten alternating multilayers with the irregularity in height with $\Delta y_{\max}=205$ nm (dotted line). The reflection spectrum for the array of ten alternating multilayers was obtained by averaging five series of calculations.

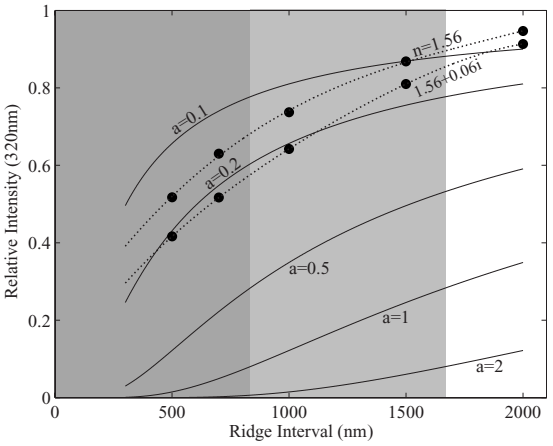

FIG. 18. Ridge-interval dependence of angle-integrated reflection intensities at 320 nm, which are divided by the total number of model structures (closed circles with dotted lines). The data were obtained for ten alternating multilayers with a height irregularity of $\Delta y_{\max}=205$ nm and refractive indices for the cuticles of 1.56 and $1.56+0.06i$, respectively. The solid lines were calculated using Eq. (10) with various values of a. The unshaded, weakly shaded, and heavily shaded areas indicate that light being emitted toward $\phi=64°$ suffers from no scattering, scattering from one ridge, and scattering from more than two adjacent ridges, respectively; these were estimated geometrically.

between ten ridges and a single ridge. The result is shown in Fig. 18, where the intensity ratio at 320 nm is plotted for ten ridges against a single ridge. As expected, the relative reflection intensity at around 320 nm notably decreases when the ridge interval is decreased. Since the reflection at around 320 nm emits light toward ~64° judging from Fig. 15, this means that the reflection at large angles is considerably reduced.

We tentatively analyzed these data using a simple continuum model in which ridges and the spaces between them are assumed to be expressed as a continuous medium; the medium has an average property that is inversely proportional to the ridge interval l. The intensity of light propagating within this continuous medium suffers from scattering or absorption due to the adjacent ridges, which obeys the usual Lambert-Beer rule and is expressed by

$$T_1 = \exp[-(a/l)(d_m/\cos\theta_1)]/N_r, \tag{10}$$

where we assume that the propagating light is directed toward the reflection angle of θ_1 which is emitted from the effective height of the ridge d_m; d_m is evaluated at half of the ridge height by using the formula $d_m=d(M-1)/2$. Here, a is a proportional constant, N_r is the number of ridges, and θ_1 is taken as 64° in this case. For simplicity, we neglected the refraction and reflection at the surface of the continuous medium. We plotted T_1 with varying l as shown in Fig. 18. The transmittance evaluated by Eq. (10) shows a remarkable decrease as the ridge interval decreased. It seems that at around the value of $a=0.2$, the curve at least partly reproduces the NS-FDTD calculations in a region where the ridge interval is smaller. Thus, the intensity of light passing through adjacent ridges should reduce to $1/e$ when it passes through approxi-

mately five ridges. This discussion also explains why the reflection spectra for ten ridges and a single ridge are not so different in the TE mode. In the TE mode, the reflection to larger angles is strongly suppressed owing to a dipole induced by incident light that is directed transversely within a plane of incidence.

We also calculated the case for when the refractive index of cuticle does not have an imaginary part. The result is also shown in Fig. 18. Although a slight increase in the reflection intensity was observed, the tendency was quite similar to that with the imaginary part. This means that up to the magnitude of an imaginary part of 0.06, the loss of light passing through adjacent ridges mostly originates from the scattering of light, which anyway contributes to the transmission of light through an array of ridges.

On the other hand, the continuum model overestimates the effect when the ridge interval is sufficiently large. In fact, a simple geometrical consideration shows that no effect is expected when the ridge interval is larger than $l=d_m \tan \theta_1 = 1680$ nm, which is the white zone in Fig. 18; between $d_m \tan \theta_1/2 = 840$ and 1680 nm, only one-time scattering takes place. Thus, the deviation found in large ridge intervals in the continuum model is partly explained by this geometrical consideration.

VI. DISCUSSION

Many important conclusions were derived from the NS-FDTD calculations in this study, which are summarized as follows:

(1) In spite of the presence of considerable irregularity and limited sampling, ridge structures obtained by binarizing TEM data reproduce the reflection spectrum fairly well when light reflected to all the reflection angles is integrated. We noticed that the obtained spectrum was slightly different from that calculated for a single ridge clipped from TEM data.

(2) Under normal incidence, a flat multilayer shows strong reflection toward the normal direction, suggesting that multilayer interference provides a considerable contribution. Decreasing the difference between the refractive indices of the cuticles and air resulted in good agreement with the analytical model proposed by Kinoshita *et al.* [25], which clarified the limited applicability of the analytical model.

(3) The reflection properties of alternating multilayers, including tree-shaped multilayer, are characterized both by the strong suppression of reflection toward the normal direction and by a prominent angular shift of the reflection with the wavelength. This suggests that multilayer interference is strongly suppressed, and a diffraction grating constructed by longitudinally repeating layers gives a major contribution. Thus, alternating multilayers basically enhance the reflection at short wavelengths with large reflection angles by sacrificing the reflection toward the normal direction.

(4) The reflection properties of a regular array of alternating multilayers are characterized by diffraction spots whose intensities are modulated by angle-dependent reflection intensities of a single alternating multilayer. This gives apparent peaks in angle-integrated reflection spectrum, which are explained in terms of overlapping the angular dependence of a diffraction grating and a single ridge structure.

(5) If irregularity is introduced in the height of alternating multilayers, the reflection to larger angles is strongly suppressed and the spectral shape becomes different from that expected from a single alternating multilayer. This suppression comes from the scattering of reflected light by adjacent structures, which is particularly prominent for the TM mode since the reflection directions are distributed over a wide angular range. As a consequence, the reflection spectrum in the TM mode is considerably affected by the scattering due to adjacent ridges, which prevents reflection at shorter wavelengths. On the other hand, the TE mode is fairly unaffected by adjacent ridges, and the reflection spectrum seems to be solely determined by a single alternating multilayer. Thus, a clear difference in mechanisms between the two polarizations was expected, even though the obtained spectra are similar to each other.

The above results may provide a simple hypothesis for producing *Morpho* blue. If one attempts to produce the *Morpho* blue with a reflection peak wavelength located in a blue region and with a moderate spectral width, it is convenient to make a multilayer using a material with appropriate refractive indices. However, if the width of the multilayer is infinitely long so that only specular reflection occurs, this is not adapting a biological purpose to make the butterfly conspicuous. It is possible that the angular range of the reflection can definitely be broadened simply by shortening the width of the multilayer and by introducing irregularity in the height.

However, instead of simply doing this, *Morpho* butterfly actively destroys multilayer interference by introducing an alternating structure to attain destructive interference toward the normal direction. This necessarily makes the angular range extraordinarily wider and hence increases the reflection at short wavelengths. In the TE mode, this does not have much of the affect because the angular range is originally limited by dipole radiation. On the other hand, in the TM mode, where the angular range of dipole radiation is essentially uniform within an incidence plane, a considerable enhancement of the short-wavelength component is expected, which results in a large polarization difference in the reflection spectrum. The wavelength selectivity of the reflection in the TM mode also becomes quite low. The increase in the density of ridges is quite convenient for reducing this effect through only the scattering of the large reflection-angle component in the TM mode, in addition to the ordinary enhancement of the overall reflectivity. Thus, although essentially similar spectra are obtained for both polarizations, the restrictions in the angular range are governed by completely different mechanisms.

In this study, we showed that the alternating multilayer is a method to modify the angular range of the reflection, which *Morpho* butterflies acquired over the long course of evolution. This structure actively destroys the multilayer interference toward the direction of specular reflection and largely enhances the character of a diffraction grating due to longitudinally repeating shelves; these shelves cause the reflection to large angles that accompany the shift of the major reflection band to shorter wavelengths. In this sense, a simple flat multilayer with very narrow width may also give essentially

the same result because the narrow width necessarily reduces the character of multilayer interference and enhances that of diffraction grating as shown in Fig. 8.

However, we speculate that there is an essential difference between a simple flat multilayer with narrow width and an alternating multilayer: the response to obliquely incident light. In an alternating multilayer, the alternately stacked shelves constitute obliquely aligned lamellae on both sides of the ridge, which strongly enhances backscattering of light toward the incident direction when the incident angle coincides with the inclination angle of the oblique lamellae, as implied by Berthier *et al.* [30]. A similar effect cannot be expected for a flat multilayer even if the width of the multilayer is sufficiently small. The presence of backscattering in these types of fauna is extremely beneficial for showing their colors clearly when there is an absence of specular reflection with no color selectivity. We are now investigating the optical response of similar alternating structures under various incidence angles and wavelengths. The results will soon be published elsewhere.

[1] M. Srinivasarao, Chem. Rev. (Washington, D.C.) **99**, 1935 (1999).
[2] P. Vukusic and J. R. Sambles, Nature (London) **424**, 852 (2003).
[3] S. Kinoshita and S. Yoshioka, *Structural Colors in Biological Systems—Principles and Applications* (Osaka University Press, Osaka, 2005).
[4] S. Kinoshita and S. Yoshioka, ChemPhysChem **6**, 1442 (2005).
[5] A. R. Parker and N. Martini, Opt. Laser Technol. **38**, 315 (2006).
[6] S. Berthier, *Iridescences—The Physical Colors of Insects* (Springer, New York, 2006).
[7] S. Kinoshita, S. Yoshioka, and J. Miyazaki, Rep. Prog. Phys. **71**, 076401 (2008).
[8] S. Kinoshita, *Structural Colors in the Realm of Nature* (World Scientific, Singapore, 2008).
[9] L. Rayleigh, Philos. Mag. **37**, 98 (1919).
[10] A. A. Michelson, Philos. Mag. **21**, 554 (1911).
[11] Lord Rayleigh, O.M., F.R.S., Proc. R. Soc. London, Ser. A **93**, 565 (1917).
[12] C. W. Mason, J. Phys. Chem. **31**, 321 (1927).
[13] E. Merritt, J. Opt. Soc. Am. **11**, 93 (1925).
[14] H. Onslow, Phil. Trans. **211**, 1 (1923).
[15] F. Süffert, Z. Morphol. Oekol. Tiere **1**, 171 (1924).
[16] T. F. Anderson and A. G. Richards, Jr., J. Appl. Phys. **13**, 748 (1942).
[17] K. Gentil, Z. Morphol. Oekol. Tiere **38**, 344 (1942).
[18] H. Ghiradella, Ann. Entomol. Soc. Am. **77**, 637 (1984).
[19] H. Ghiradella, *Microscopic Anatomy of Invertebrates* (Wiley-Liss, New York, 1998), Vol. 11A, p. 257.
[20] H. Ghiradella and W. Radigan, J. Morphol. **150**, 279 (1976).
[21] H. Ghiradella, Microsc. Res. Tech. **27**, 429 (1994).
[22] W. Lippert and K. Gentil, Z. Morphol. Oekol. Tiere **48**, 115 (1959).
[23] L. Bingham, I. Bingham, S. Geary, J. Tanner, C. Driscoli, B. Cluff, and J. S. Gardner, Microsc. Res. Tech. **31**, 93 (1995).
[24] P. Vukusic, J. R. Sambles, C. R. Lawrence, and R. J. Wootton, Proc. R. Soc. London, Ser. B **266**, 1403 (1999).
[25] S. Kinoshita, S. Yoshioka, and K. Kawagoe, Proc. R. Soc. London, Ser. B **269**, 1417 (2002).
[26] S. Kinoshita, S. Yoshioka, Y. Fujii, and N. Okamoto, Forma **17**, 103 (2002).
[27] S. Yoshioka and S. Kinoshita, Proc. R. Soc. London, Ser. B **271**, 581 (2004).
[28] S. Yoshioka and S. Kinoshita, Proc. R. Soc. London, Ser. B **273**, 129 (2006).
[29] L. Plattner, J. R. Soc., Interface **1**, 49 (2004).
[30] S. Berthier, E. Charron, and A. Da Silva, Opt. Commun. **228**, 349 (2003).
[31] S. Wickham, M. C. J. Large, L. Poladian, and L. S. Jermiin, J. R. Soc., Interface **3**, 99 (2006).
[32] S. Berthier, E. Charron, and J. Boulenguez, Insect Sci. **13**, 145 (2006).
[33] S. E. Mann, I. N. Miaoulis, and P. Y. Wong, Opt. Eng. **40**, 2061 (2001).
[34] A. M. Young, Oecologia **7**, 209 (1971).
[35] P. K. C. Pillai, J. Opt. Soc. Am. **58**, 1019 (1968).
[36] H. Tabata, K. Kumazawa, M. Funakawa, J. Takimoto, and M. Akimoto, Opt. Rev. **3**, 139 (1996).
[37] R. O. Prum, T. Quinn, and R. H. Torres, J. Exp. Biol. **209**, 748 (2006).
[38] J. J. Cowan, J. Opt. Soc. Am. A **7**, 1529 (1990).
[39] B. Gralak, G. Tayeb, and S. Enoch, Opt. Express **9**, 567 (2001).
[40] S. Banerjee, J. B. Cole, and T. Yatagai, Micron **38**, 97 (2007).
[41] G.-P. Liu, Y.-M. Xuan, and Y.-G. Han, Acta Laser Biol. Sinica **15**, 511 (2006).
[42] K. Jin, X.-X. He, and R.-S. Chen, J. Nanjing Univ. Sci. Technol. **31**, 118 (2007).
[43] T. Uno, *Finite Difference Time Domain Method for Electromagnetic Field and Antenna Analyses* (Coronasha, Tokyo, 1998).
[44] R. J. Luebbers, D. Ryan, and J. Beggs, IEEE Trans. Antennas Propag. **40**, 848 (1992).
[45] *Applications of Nonstandard Finite Difference Schemes*, edited by R. E. Mickens (World Scientific, Singapore, 2000).
[46] A. Taflove and S. C. Hagness, *Computational Electrodynamics: The Finite-Difference Time-Domain Method* (Artech House, Boston, 2005).
[47] J. B. Cole, IEEE Trans. Microwave Theory Tech. **45**, 991 (1997).
[48] J. B. Cole, in *Applications of Nonstandard Finite Difference Schemes*, edited by R. E. Mickens (World Scientific, Singapore, 2000), pp. 109–153.
[49] J. B. Cole, IEEE Trans. Antennas Propag. **50**, 1185 (2002).
[50] M. Kambe, Ph.D. thesis, Osaka University, 2009.